Accepted Manuscript

Rusty river: Effects of tufa precipitation on sediment entrainment in the Estero Morales in the central Chilean Andes

Diego Ravazzolo, Luca Mao, Cristian Escauriaza, Pablo Pastén, Mauricio Montecinos

PII: S0048-9697(18)34183-4
DOI: doi:10.1016/j.scitotenv.2018.10.287
Reference: STOTEN 29190

To appear in: *Science of the Total Environment*

Received date: 28 May 2018
Revised date: 17 October 2018
Accepted date: 21 October 2018

Please cite this article as: Diego Ravazzolo, Luca Mao, Cristian Escauriaza, Pablo Pastén, Mauricio Montecinos , Rusty river: Effects of tufa precipitation on sediment entrainment in the Estero Morales in the central Chilean Andes. Stoten (2018), doi:10.1016/j.scitotenv.2018.10.287

Rusty river: effects of tufa precipitation on sediment entrainment in the Estero Morales in the central Chilean Andes

Diego Ravazzolo[1, *], Luca Mao[1, 2, 3], Cristian Escauriaza[3, 4], Pablo Pastén[4, 5], Mauricio Montecinos[4, 5]

[1]Department of Ecosystems and Enviroment, Pontificia Universidad Católica de Chile, Santiago, Chile

[2]School of Geography, University of Lincoln, Lincoln, UK

[3]Centro de investigación para la gestión integrada de desastres naturales (CIGIDEN), Santiago, Chile

[4]Department of Hydraulic and Environmental Engineering, Pontificia Universidad Católica de Chile, Santiago, Chile

[5]Centro de Desarrollo Urbano Sustentable (CEDEUS), Santiago, Chile

[*]Corresponding author: diravazzolo@uc.cl

Abstract: Rivers and streams continuously shape and reform their channels through the transport of sediment. One of the most important parameter used to assess this transformation is the threshold for incipient grain motion. To date, limited studies have reported that several biotic and abiotic factors can affect this parameter. However, the effects of tufa precipitation on sediment entrainment and dynamics are still unexplored. The Estero Morales is an Andean stream in Central Chile affected by the phenomenon of tufa precipitation during the winter. Along the wetted channels, tufa precipitate creates a thin solid layer that covers the sediments. A series of field surveys and flume experiments were conducted to analyze the effect of tufa precipitation on the initiation of motion and sediment dynamics. Along the wetted areas of the river, a portable dynamometer was used to explore the force needed to dislocate the grains affected by tufa precipitation from the surrounding sediments. Flume experiments were conducted to compare the incipient motion of sediment covered by tufa precipitation with unaffected sediment. Geochemical analyses were conducted to study the precipitate chemistry, mineralogy and texture. The results demonstrate that greater force is needed to move sediment particles affected by tufa precipitation compared to unaffected ones. In addition, lower sediment transport rates were measured on sediment affected by tufa precipitation, especially for the largest sediment size. These results could have important implications for studies concerning sediment dynamics and contaminant fate

in the environment. Moreover, the results allow us to make some assumptions regarding the long-term role that tufa precipitation can play in rivers.

Such analysis can help us to better understand and predict the changes in sediment transport rates due to tufa precipitation.

Keywords: tufa precipitation, sediment dynamics, flume experiments, geochemical analysis, Andean stream, central Chile

Rusty river: effects of tufa precipitation on sediment entrainment in the Estero Morales in the central Chilean Andes

1. Introduction

The morphology and morphodynamics of river systems are determined by the motion of sediments, which is the foundation of fluvial processes and dynamics. A key parameter needed to assess coarse sediment transport is the threshold conditions at which sediments of different sizes are entrained. The pioneering experimental study on this topic was conducted by Shields (1936), who related the Reynolds conditions of the flow with dimensionless shear stress. For fully turbulent flow and noncohesive sediments, grains are expected to move when the dimensionless shear stress is higher than a critical threshold, which is approximately 0.06 for wide fully rough conditions. A subsequent investigation revealed that this critical threshold is severely affected by the way in which incipient motion is defined and assessed in flume or field studies and by other sources of uncertainty (such as sediment mixtures, grain shape, orientation, exposure, and protrusion). The values of dimensionless shear stress typically range from 0.03 to 0.08, depending on the investigative methodology (e.g., Buffington and Montgomery, 1997). For instance, the critical bed shear stress needed to entrain coarse sediments decreases with increasing bed slope (Shvidchenko et al., 2001; Lamb et al., 2008) and is strongly affected by the relative

submergence of the grains (Bathurst et al., 1987) and decelerating flows (Bolhassani et al., 2015). Additionally, apart from the influence of grain size (e.g., Kuhnle, 1993), the incipient sediment motion is further dependent on the surface organization, clustering, and protrusion of the coarser grains (Schmeeckle and Nelson, 2003; Lee and Balachandar, 2012). Despite the remarkable uncertainty in sediment entrainment due to the physical factors mentioned above, a considerable body of research has been recently devoted to the role that biota can exert on fluvial geomorphological processes, especially sediment motion (Naiman et al., 2000; Pledger et al., 2014; Piqué et al., 2016). Rice et al. (2012) demonstrated that fish and macroinvertebrates can play an important role in bed sediment stabilization or destabilization, whereas Pledger et al. (2014) showed that foraging juvenile barbel can increase grain entrainment by 82 %, resulting in higher mobility and sediment transport rates. Furthermore, Buxton et al. (2015) investigated the effects of Pacific salmon spawning on thresholds of sediment mobility and found that the threshold for sediment motion is 22 % higher in spawned beds, implying that biological factors can impact landscape evolution by increasing the sediment transport of rivers. Many studies have also recently investigated the role of bacteria and macrophytes on sediment transport. In natural rivers, sediments could be covered by biofilms that affect sediment mobility (Stone et al., 2011, Vignaga et al., 2013, Cheng et al., 2017), flow characteristics, and landform development

(Fang et al., 2017). The relationship between sediment motion and biofilm presence has been investigated in marine (Grant and Gust, 1987; Underwood and Peterson, 2003) and freshwater (Cyr and Morton, 2006; Righetti and Lucarelli, 2007) environments. It has been demonstrated that five times higher shear stress is required to entrain marine sediment influenced by benthic microbiota compared to unaffected sediment (Grant and Gust, 1987). Vignaga (2012) showed that natural biofilms increase the critical shear stress of sediment entrainment by up to 21 %. Biofilms can also change boundary flow properties (Stone et al., 2011), especially because reduced surface roughness tends to accelerate mean flow velocity, changing the turbulence intensity and thus affecting sediment erosion (Graba et al., 2010; Gerbersdorf and Wieprecht, 2015, Thom et al., 2015). Overall, biofilms tend to increase sediment stability (Righetti and Lucarelli, 2007; Gerbersdorf et al., 2008; Fang et al., 2014) and reduce sediment transport rates (Stone et al., 2011; Piqué et al., 2016). For instance, Fang et al. (2014) observed that the incipient velocity needed to entrain sediments in a laboratory experiment increased by approximately 60 %, 70 %, 45 %, and 40 %, after two, four, six, and eight weeks of biofilm colonization, respectively. Moreover, Piqué et al. (2016) visually noted that sediments colonized by biofilms in a flume experiment have a delay in entrainment compared with unaffected sediments. Lundkvist et al. (2007) further showed

that combined algal and microbial biofilms increased sediment stability by 150 % over physicochemical binding alone.

Similar to fish, macroinvertebrates and biofilms, the precipitation of calcium carbonate ($CaCO_3$), which when precipitated in ambient conditions is called calcareous tufa, can create a concrete-like layer on grain surfaces (Pedley, 1990), with a probable influence on their entrainment and transport in rivers. Tufa is a porous sedimentary deposit (limestone) composed of calcium carbonate (Martini and Capezzuoli, 2014) that naturally occurs in rivers, lakes or springs in karst regions (Arenas et al., 2010; Toker, 2017) through degassing of CO_2 from karst groundwater (White, 2010). Tufa precipitation is more frequently observed in dolomite and dolomite-gypsum terrain springs (Ordoñez and Benavente, 2014). In naturally flowing rivers, water can lose carbon dioxide into the atmosphere or by photosynthesis and the solution becomes supersaturated with respect to calcite. Calcite precipitation is strongly dependent on pH, water temperature and ionic strength (Rupp and Adams, 1981; Lu et al., 2000). The deposition is often located in river channels downstream from springs as bulk water degases, and it may continue downstream for many kilometers (Kempe and Emeis, 1985; Drysdale et al., 2002). The essential reactions that govern calcium carbonate precipitation are:

(1) $CaCO_3 + CO_2 + H_2O \leftrightarrow (HCO_3^-)_2 + Ca^{2+}$

(2) $CO_2 + H_2O \leftrightarrow H_2CO_3 \leftrightarrow H^+ + HCO_3^-$

Calcite is controlled by temperature (1): calcite and CO2 solubility in water is higher in cool conditions and the saturation index increases as temperature increases and CO2 is lost from water (2) raising the pH.

Tufa precipitation might retain contaminants from the water, where they remain stored until flushed by exceptional storms (White, 2010). Tufa is usually produced in rivers with cold water (< 20° C; Pedley, 1990) and high calcium bicarbonate concentration (Capezzuoli et al., 2014), and it is also generally subject to seasonal oscillations due to changes in air or water temperature (Vázquez-Urbez et al., 2010). Moreover, Ford and Pedley (1996) used the term tufa for deposits containing the remains of plants, animals and bacteria. However, tufa depositional environments are quite variable, and fluvial and lithoclastic deposits may be found in association with paludal tufa as a result of occasional high water levels (Arenas et al., 2000; Carthew et al., 2003; Arenas et al., 2014; Toker, 2017). Pedley (1990) suggested that four model types should be considered: spring, paludal, lacustrine and fluvial. Arenas et al. (2010) indicated that the formation of fluvial carbonate deposits can be due to several external (bedrock configuration, climate, tectonic) and internal (presence of vegetation, chemical and physical properties of water, etc.) factors. Tufa frequently contains translucent and equant calcite crystals (sparry) and microcrystalline calcite (microspar) (Turner et al., 2000), as well as microphytes and cyanobacteria. Facies such as oncoids, stromatolites, and coatings of

macrophyte stems display several micrometer to 1-1.5 cm thick layers distinguished by color, crystal size, thickness, porosity and/or biological components. The typical sedimentary environment is characterized by fast flowing water. The stromatolite morphology also depends on physiographic conditions such as water depth and slope (Carthew et al., 2003). Stromatolite-like forms may develop in a channel (Pedley, 1990; Arenas et al., 2000), typically with an asymmetrical flow-aligned morphology (Carthew et al., 2003) and can be composed of laminae up to 1 mm thick that occurs parallel to the flowing current (Toker, 2017). However, layers can accumulate and deposits can build up to meter-scale mounds (Riding, 1979). Some authors associate the formation of stromatolites with cyanobacteria and algae (Pedley, 2009; Gradziński, 2010; Pedley, 2014).

Despite some insight into the role of tufa precipitation on sediment dynamics in rivers, this topic is still almost uninvestigated. The aim of this study is to quantify the role of tufa precipitation in sediment entrainment and transport in the main channel of an Andean stream (Estero Morales). This stream is affected by this kind of precipitation, which creates a solid layer that covers sediments in winter. The study was conducted both in the field and in a set of flume experiments. Field surveys were primarily conducted to examine the force needed to remove grains affected by tufa precipitation. Flume experiments were designed to explore the incipient motion difference of sediment covered by a tufa precipitation layer versus

sediments of similar size without tufa precipitation. A basic characterization of the water and precipitate geochemistry was conducted by in situ measurements, laboratory analyses, and thermodynamic calculations.

The specific objectives are, therefore, to i) determine how tufa precipitation effects sediment entrainment and transport; ii) analyze the effects of tufa precipitation on bed stabilization, measuring the force needed to dislodge and remove a grain covered by tufa; iv) review the evidence, discussing it in terms of the potential implications of tufa precipitation for river processes, evaluating a progressive reduction in the glacier surface, and the projected increase in temperature, which are global trends in glaciered environments such as the Estero Morales.

2. Geological setting

The study was carried out in the Estero Morales, a high-gradient stream of the central Chilean Andes (33°49'19.9''S–70°03'46.5''W). The basin drains an area of 27 km^2 and flows into the Maipo River, which eventually flows into the Pacific Ocean. The basin ranges in elevation from 3815 m to 1850 m a.s.l., and it hosts several small glacial bodies in its upper part, some covered by debris and some hanging on the steep rocky slopes, for an overall area of 1.8 km^2. The mainly geologic composition of the Estero Morales basin consists of volcano-metamorphic rocks and conglomerate-sand deposits originated by gravitation and moraines (Vacca et al., 2016). The larger glacier is called San Francisco and it melts from December to

March providing a summer season with significant daily fluctuations of discharge, ranging from approximately 0.8 m^3 s^{-1} to 2.3 m^3 s^{-1}. The mean annual rainfall (measured at a station nearby at 2475 m a.s.l.) is approximately 570 mm occurring mainly during the winter from May to September. Further details on the flow regime and sediment transport dynamics are provided in Mao et al. (2016) and Mao and Carrillo (2017).

3. Materials and methods

3.1 Study site

A series of field surveys were carried out in the lower portion of the Estero Morales before the confluence with the Volcán River. The study site is characterized by a width and depth of approximately 5 m and 0.5 m, respectively. The site is confined and steep (0.14 m m^{-1}) with coarse sediments and cascade/step-pool morphology (Figure 2). The study site is approximately 2.5 km from a spring area called “Aguas Panimávidas”, where warm groundwater emerges on the surface creating a solid layer of precipitates (Figure 1e). In winter, the wetted surfaces of the sediments in the main channel begin to develop a solid layer with a distinct golden color from the beginning of autumn (April) that persists until spring (November) (Figure 1). The solid layer was observed by the authors over the past four years, and local residents recall having seen it during all winters in the recent past.

In the study site a day/night camera was installed on the side of the river for all of 2015. The camera was set to take a photo every hour from December 2014 until November 2015. The photos allowed us to observe changes in the channel of Estero Morales.

3.2 Sediment entrainment test in the field

The layer of tufa precipitation covering the surface sediments of the bed within the wetted area of the main channel appeared solid and compact to the touch. Because the layer was spread over all the sediments, a field procedure was applied in order to verify its effect on sediment entrainment. A digital push/pull gauge dynamometer (HF-200 manufactured by Vetus Instruments) measured the peak push force needed to move sediments. This procedure was applied on 240 sediment particles during the three field visits of September 2017 when water discharge was low (approx. 1.5 m^3 s^{-1}). Once moved, the grains were placed in the very same position, and the peak push force needed to entrain them a second time was measured again. Hence, the peak push force needed to dislodge a sediment particle with and without the tufa layer sticking them to the surrounding particles was compared. The gauge dynamometer has an accuracy of ~0.5 % and a resolution of 0.001 N. After the second dislodgement test, the three diameters and the weight of each grain were measured in the field using a caliper and a small scale, respectively.

3.3 Laboratory sediment entrainment tests

A laboratory-based method was used to quantify the effect of the tufa precipitation layer on sediment entrainment. A total of sixteen boxes made up of steel perforated metal panels (0.30 m long, 0.25 m wide, and 0.12 m deep; Figure 2) were filled with sediments of four different granularities. Three mixtures were relatively well-sorted (standard deviation of the grain size curves σ always lower than 1.1) with D_{50} of 4, 8, and 16 mm, respectively. Additionally, one poorly sorted mixture was produced by combining the homogeneous sizes to obtain a mixture with D_{50} of 9.6 mm (hereafter approximated to 10 mm) and σ of 1.7. The boxes were placed along a ~200 m reach of the main channel of the Estero Morales. The boxes were always completely submerged and were located in areas of reduced turbulence to avoid sediment movement inside the boxes (Figure 2). Two boxes were installed in July and an additional 16 were placed in the Estero Morales in August 2017. The boxes were recovered in September 2017. Special attention was paid to careful handling and transportation to avoid mechanical disruption. The boxes were slowly removed from the bed, placed in a plastic box filled with stream water, and transported to the laboratory at the Department of Hydraulic and Environmental Engineering of the Pontificia Universidad, Católica de Chile. Upon arrival at the laboratory, the sediments in the boxes were carefully inspected to detect

damage to the surface sediment layer. As a result, only nine boxes were used for the flume experiments (Table 1).

The experiments were carried out in a 10-m-long, 0.4-m-wide tilting flume. The bed was equipped with a false bed of polystyrene, artificially roughened by gluing a 4-8-16 mm mixed sediment layer on the surface. The thickness of this artificial bed was equal to the height of the metal boxes (0.12 m), and a gap able to host the box was produced at 7 m from the upstream end of the flume (Figure 2). The downstream adjustable flume weir was laid flat to allow the flow depth to adjust naturally. The water level was measured at three locations along the flume. The water was recirculated, and the inflow discharge was measured with a triangular weir located at the outlet of the flume. Each experiment consisted of several subsequent approximately 30-min long runs, in which the discharge was progressively increased by approximately 0.003 $m^3 s^{-1}$ until all surface sediments were removed from the box by the flow. Overall, runs were conducted with discharge ranging from 0.001 $m^3 s^{-1}$ to 0.055 $m^3 s^{-1}$, the slope was varied from 0.5 to 1.5 %, and the Reynolds number ranged from approximately 2300 to 85000. The detailed experimental design is presented in Table 1.

The sediments in the box were observed through the glass wall of the flume, and a camera was used to capture a video of each run. At the end of the experiments, the tufa was washed from the sediments in each box, and the sediments were then replaced into the same box. Thus, the boxes with

sediments lacking tufa precipitation were used to repeat the experiments described above, using the same run durations, discharge, and slope as for the boxes with the layer of freshwater tufa precipitation. This procedure allowed us to compare sediment entrainment and motion in boxes with and without the layer of freshwater tufa precipitation. The videos for each run were analyzed to obtain the number of particles entrained over time. The same operator always performed the counting in order to minimize errors. A particle was considered entrained when its motion exceeded approximately twice its diameter.

For each run, the shear stress (τ) acting on the bed was calculated as $\tau = (h\ S\ \rho\ g)$, where S is the measured slope, h is the water depth, ρ is water density, and g is the acceleration due to gravity. To enable direct comparison between experiments conducted using different boundary conditions, the dimensionless shear stress or Shields parameter (τ^*) was calculated as:

$$\tau^* = \frac{\tau}{(\rho_s - \rho)\ g\ D}$$

where D is the size of sediments in the box and ρ_s is the density of sediments.

The number of particles removed over the duration of a run was multiplied by the weight of particles within that size range. This was used to calculate the volumetric transport rate per unit width q_s (in g m^{-1} s^{-1}). To enable direct

comparison between different experiments, we calculated the dimensionless transport rate (q^*) as:

$$q^* = \frac{q_s}{\sqrt{(\rho_s - \rho)\ g\ (D)^3}}$$

3.4 Physicochemical analyses

Six field surveys (one in July, two in August, and three in September) were carried out in 2017 in the Estero Morales to measure in situ physicochemical parameters and to collect water and solid samples. A handheld multiparameter probe (YSI 6050000 Professional Plus) was used to measure temperature, pH, electrical conductivity, ammonium, and dissolved oxygen. The probe calibration was conducted according to the manufacturer's specifications.

Eighteen water samples (three on each of the six field surveys from July to September 2017) were collected from the stream in clean 300 ml bottles and taken to the laboratory under cool conditions (< 10° C) for prompt analysis. Several clasts covered by the tufa layer were collected during each campaign and stored in a clean plastic container. The precipitate was removed carefully with a clean spatula and dried at 40° C, obtaining at least 3 g (dry weight) for mineralogical analyses. Additionally, dried solid was digested in a microwave (Mars Microwave System, 209 MarsXpress, CEM, Matthews, USA) according to the EPA method 3051A (EPA, 2007a). Water

samples were collected in each field campaign (six field surveys in 2017). For total metal analyses samples were stored in 50 mL polypropylene tubes and acidified to pH < 2 with HNO_3 (1:1 v/v, EMSURE, Merck, Germany). Acidified samples were digested in a microwave (Mars Microwave System, 209 MarsXpress, CEM, Matthews, USA) according to the EPA method 3015A (EPA, 2007b). For dissolved metals, samples were filtered (0.45 μm cellulose acetate membrane, Merck Millipore) and acidified to pH < 2 with HNO_3 (1:1 v/v, EMSURE, Merck, Germany). Samples for Total Organic Carbon (TOC) analyses were stored in 150 mL glass bottles and acidified to pH < 2 with H_3PO_4 (1:1 v/v, EMSURE, Merck, Germany). Filtered samples (0.22 μm MCE filters, Merck Millipore) were stored at 4°C for anion analysis. Total alkalinity was measured with an automatic titrator (Titrino, Metrohm, Switzerland). TOC analyses were performed with a total organic carbon analyzer (TOC-LCPH, Shimadzu, Japan) as described by Arce et al. (2017), adapted from Bauer and Blodau (2009). Metal analyses were conducted with inductively coupled plasma optical emission spectrometry (ICP-OES, Optima 7300 V, Perkin Elmer, USA). Total reflection X-ray fluorescence (TXRF) analyses were performed with a Picofox S2 spectrometer (Bruker AXS, Germany) as described by Bugueño et al. (2014). The identification of crystalline mineral phases in the precipitate was done with X-ray diffraction (XRD) on micronized samples with a diffractometer (D2 Phaser, Bruker AXS, Germany) at 30 kV and 10 mA

using Cu-K(alpha) radiation. Samples were micronized with a mill using agate grinding elements (McCrone Micronising Mill, Westmont, IL, US). Fourier transform infrared (FTIR) spectra were collected (Prestige 21, Shimadzu, Japan) with KBr as a carrier. Anions were analyzed by ion chromatography (882 Compact IC Plus, Metrohm, Switzerland). In addition, small portions of tufa were sampled, dried to the critical point and coated with gold for study under a scanning electron microscope (SEM) coupled with an energy dispersive spectrometry (EDS) microprobe that reports the atomic composition percentage based on an average of 10 measurements. The FEI Quanta 250 scanning electron microscope with field emission and EDX was operated at 10 and 20 kV. Thermodynamic calculations were performed with the USGS PHREEQC 3.4 package (Parkhurst and Appelo 2013), which estimates the saturation index of different minerals under homogeneous equilibrium conditions using the measured water chemistry and temperature. The quality of the obtained analytical data for water samples was considered acceptable when the error in the charge balance ranged inside ± 5-10 %.

4. Results

4.1 Evidence of sediment entrainment

Overall, the force needed to remove 240 grains with and without tufa precipitation on their surface was measured. The grains that were surveyed

ranged from 11 mm to 144 mm in size and from 2 g to 3103 g in weight. The peak push force needed to dislodge and remove the grains covered by the tufa precipitation layer ranged from 0 N to 8 N, with a median value of 1.35 N. After the first move, without the sticking effect of the tufa, and exactly replaced in the same position, the grains were entrained by exerting a peak push force ranging from 0 N to 3 N, with a median value of 0.52 N (Figure 6). A Mann–Whitney U test revealed that the median value of push force needed to entrain sediments with and without the tufa precipitation layer was statistically significant ($p < 0.0001$).

The difference of peak push forces (Δ) between with and without a tufa precipitation layer needed to entrain sediments was also calculated. If sediments aggregate following their grain size in 0.5 Φ classes, the results show that the tufa precipitation layer exerts greater effect on the entrainment of coarse grains (Figure 7). When covered by the freshwater tufa precipitate layer, sediments finer than 45 mm required, on average, 1.5 N more force to be dislodged, with several grains requiring approximately 6 N more force. For the coarser grains (up to 144 mm), the additional force required for their entrainment is approximately 2.5 N with some grains requiring up to 8 N of additional force (Figure 7). An independent samples t-test confirms that the difference between classes is statistically significant ($p < 0.05$).

4.2 Results of flume experiments

Figure 8 shows the relationship between the sediment transport rate (in terms of q^*) and the dimensionless shear stress (τ^*) for each experiment. Apart from the obvious transport rate increase with shear stress, the value of shear stress at which sediment transport becomes observable (i.e., the critical conditions for sediment motion) ranges between 0.04 and 0.06. Figure 8 shows that in three cases (8-a, 16-b, 10-b) there were lower sediment transport rates for sediments affected by tufa precipitation than those unaffected. Tufa precipitation appears to be more effective in determining the sediment transport rate of coarser sizes. In fact, the largest difference was registered for experiments 8-a and 10-b, in which higher sediment transport rates were observed for more than 90 % of the unaffected sediment over the total experiment time. This result is in agreement with what was observed in the field (Figure 7). Assuming an arbitrary critical incipient motion value of τ^*_c = 0.056, the percent difference of sediment transport rate between the samples with and without the tufa precipitate layer was calculated (Figure 9). The difference in sediment transport rate at that value of shear stress is generally 80 % higher without the layer of tufa precipitation, and in two cases is up to nearly 300 % higher. Figure 9 shows that this result is irrespective of grain size and confirms what was also observed in the field for finer sizes (Figure 7).

Figure 10 shows the sediment transport flux over time for experiment 16-b for sediments with and without the tufa precipitation layer. The sediment

flux was twice as high for sediment without tufa as for sediments covered by tufa precipitate. Experiments 16-b, also 8-a, 8-c, 10-a and 10-b reported less accumulated sediments moving over time for those affected by tufa precipitation than the unaffected. This trend was not verified for the finest sediments. Approximately 40 % higher sediment flux was entrained for tufa affected grains in experiment 4-a with almost the same sediment entrainment for experiment 4-b.

4.3 Physicochemical analyses

Water samples taken between July and September 2017 showed the following physicochemical parameters: pH: 7.7 ± 0.4 (7.1 - 8.2); temperature (°C): 5.3 ±1.5 (3.4 - 6.6); conductivity (µS cm^{-1}): 491 ± 55 (421 - 551); turbidity (NTU): 24.3 ± 10.4 (10.5 - 40.4); TOC (mg l^{-1}): 0.22 ± 0.05 (0.16 - 0.27); total alkalinity (mg l^{-1} as $CaCO_3$): 186 ± 27 (136 - 207); ions (mg l^{-1})); Al_{total}: 0.54 ± 0.53 (0.11 – 1.52); Ca_{total}: 140 ± 14 (118 - 160); Fe_{total}: 0.76 ± 0.49 (0.30 - 1.72); K_{Total}: 1.4 ± 0.1 (1.3 - 1.6); Mg_{total}: 20 ± 2 (16 - 23); Mn_{total}: 0.16 ± 0.02 (0.13 - 0.19); Na_{total}: 8.7 ± 1.0 (6.9 - 9.5); NH_4 (mg l^{-1}): 0.01 ± 0.005 (0.01 - 0.02); Cl^-: 1.3 ± 0.3 (0.9 - 1.8); SO_4^{2-}: 202 ± 47 (139 - 269); DO (mg l^{-1}): 5.5 ± 1.6 (3.46 - 8.01). Calcium and sulfate (Ca^{2+} ~ 50 %; SO_4^{2-}: 35 %) were the largest contributors to the water ionic strength ranging between 0.010 and 0.016 M. The calcite saturation index ranged between -0.2 (subsaturation) and 0.9 (supersaturation) except the

field campaign on 09/08/2017 when pH reached the lowest value (7.1), whereas for Fe solid phases ($Fe(OH)_3$, goethite) the index was higher than 1. XRD of three precipitate samples (Figure 3a) shows that the dominant crystalline phase is largely calcite, agreeing with the thermodynamic calculations. FTIR confirms calcite as the main solid phase (Figure 3b). Elemental analysis of digested solid shows Ca concentration between 344 and 450 g kg^{-1}, consistent with calcite identification by XRD and FTIR. However, approximately 18 g kg^{-1} of Fe and no crystalline Fe minerals in the XRD implies an amorphous Fe phase. There is no evidence of toxic metals or metalloids of concern at high concentrations in the precipitate according to TXRF (As < 10 mg kg^{-1}; Cr < 10 mg kg^{-1}; Cu < 80 mg kg^{-1}; Pb < 5 mg kg^{-1}; V<10 mg kg^{-1}; Zn < 70 mg kg^{-1}).

Several samples of precipitates were also analyzed with SEM (Figure 4), showing a porous rough surface where spar and micrite calcite crystals of varied shapes and sizes are observed. The facies consisted of laminae mostly formed of calcite tubes (Figure 4a). The spaces among the tubes are occupied by spar and micrite calcite as well as by other microbial components (e.g., diatoms and unidentified bacteria). Bacteria are associated with the precipitate surface (Figure 4c) and they do not appear embedded in the characteristic EPS matrix of biofilms. As it is possible to observe in Figure 4d, clusters of globular nanoparticles resembling

nanosized byproducts of iron oxidation (e.g., goethite, hematite) are associated with the precipitate surface.

The SEM-EDS analysis suggests that the precipitate is mostly composed by O (62.8±3.8), Ca (19.5±5.6), C (12.2±3), Si (1.5±1.1), and Fe (1.2±1.7). Other minor components include Al, Na, K, Mg, and S, which is consistent with CaCO3 precipitate and the presence of diatoms (Si) and iron oxides (Fe), with a marginal biological component (Figure 4e).

4.4 Dynamics of tufa appearance and vanishing in the Estero Morales

The fixed camera installed on a bank of the Estero Morales allowed us to visually observe the formation and disappearance of the reddish tufa deposit overtime, from the first days of autumn (April) to the end of spring (November). Figure 11 shows some selected photos of the period, along with the continuous data of liquid discharge and conductivity. Interestingly, tufa precipitation appears when discharge is low and not able to move any sediment, and it disappears when the discharge starts increasing again in springtime with snowmelt. In addition, the period in which the visual appreciation of tufa is higher corresponds with the highest values of conductivity ever recorded (approximately 500 µS cm^{-1}).

5. Discussion

5.1 Critical entrainment

The conditions for incipient motion of sediments in rivers depend on a variety of physical factors such as flow strength, turbulence, and grain size, along with slope, sediment heterogeneity, and relative submergence as among the most important (Bathrust et al., 1987; Kuhnle, 1993; Shvidchenko et al., 2001; Lee and Balachandar, 2012). In our flume experiments, the critical dimensionless shear stress ranges between 0.04 and 0.06. This was expected, as the Shields (1936) reference value is commonly assumed to be 0.056, but subsequent studies reported values ranging from 0.03 to 0.06 (see Buffington and Montgomery, 1997; Bunte et al., 2013). However, several recent studies revealed that other factors could be crucially important in determining the incipient conditions for sediment entrainment, such as the presence of biofilms (Vignaga et al., 2013) and the activities of macroinvertebrates (Johnson et al., 2009) and fish (Gottesfeld et al., 2004). In this study, we showed that a recent layer of freshwater tufa precipitation exerts a strong effect on sediment incipient motion and bed stability. Indeed, the peak push force needed to entrain sediment particles affected by this layer increases up to 97 %. This percentage is remarkably high compared with values considering other factors that influence sediment entrainment. For example, it is approximately three times greater than that reported by Johnson et al. (2009) regarding the difference in critical shear

stress needed to entrain sediment affected by *Hydropsychidae* caddisfly larvae. Moreover, the authors reported a critical shear stress for entrainment 35 % greater for colonized sediments than the uncolonized. On the other hand, fish activity during the spawning season may even decrease the incipient motion of sediment by 22 % (Buxton et al., 2015). In addition, Vignaga (2012) cultured a phototrophic cyanobacterium typical of freshwater (*Phormidium* sp. strain PP03) over sediment samples and observed an increase of 20 % for the sediment entrainment critical shear stress. Fang et al. (2014) also reported a 40 % increase in incipient velocity after eight weeks of biofilm colonization, reaching a peak of 70 % approximately four weeks after the colonization. On the other hand, tufa precipitation seems to have less impact than the combination of algal and microbial biofilms, which may increase bed stability 150 % (Lundkvist et al., 2007). Due to the important role of tufa precipitation on threshold Shields parameters for sediment, more studies should be conducted to improve the Shields diagram for the threshold of sediment motion (Righetti and Lucarelli, 2007; Fang et al., 2014). However, in this study, for small particles (4 mm), tufa precipitation does not seem to play an important role in incipient motion. Most likely, as observed by Fang et al. (2014) analyzing the effects of biofilm on sediment motion and other forces (i.e., the cohesive) could play a more dominant role, and tufa precipitation becomes relatively insignificant. Similar observations were also reported by Vignaga

et al. (2012), who compared the adhesive strength of beads and sand affected by biofilms. They observed higher adhesive strength over beads, resulting in the greatest resistance to shear for a longer time. One of the reasons motivating the authors has been the capacity of biofilms to penetrate deeper into beads. Although a porosity effect was not observed, the same seems to apply to tufa precipitation, as its sticking effect tends to increase with the particle size. This can be observed for the experiments with sediment size of 16 mm and the mixture of 4-8-16 mm (experiments 16-b and 10-b in Figure 8) and with field surveys for particles with the greatest dimensions (Figure 7).

5.2 Physicochemical characterization of water and the tufa layer

The chemical shifts favoring precipitation and dissolution of calcite are a likely underlying chemical control for the presence of the tufa. The EDS, XRD and FTIR evidence support the presence of calcite, whereas the stream water chemistry varies between calcite subsaturation and supersaturation, as indicated by thermodynamic equilibrium calculations. The temporal variations in flow are linked to variations in electrical conductivity (Figure 11), determining higher conductivity for low flow, and lower conductivity for high flow. Higher conductivity indicates higher ionic strength associated with higher Ca^{2+} concentration according to our measurements, thus favoring calcite precipitation. Other solids may be present in minor

quantities, but they do not seem to control the chemical integrity of the bulk precipitate. Quartz is revealed by XRD, and other phases (e.g., feldspars) may be present in minor quantities, hinted by weaker XRD peaks and FTIR bands that are utilized to resolve their identity. The hydrated amorphous Fe oxyhydroxide giving the characteristic orange color to the tufa is thermodynamically stable for all conditions considering the observed pH and oxic conditions, yet it does seem to support a substantial precipitate layer. In the absence of a coprecipitating porous matrix, Fe oxyhydroxides are likely to occur as small particles with slow settling velocity that are mobilized by the bulk stream (Hamdouni et al., 2016). A preliminary analysis with SEM-EDS of the solid samples shows an association of Fe with nanoparticles (Figure 5). Ca, C, Al, and Si are also observed in the nanoparticles possibly due to surrounding areas providing fluorescence and because the nanoparticle surfaces serve to coprecipitate these elements, since everything occurs concurrently. In areas without nanoparticles, little or no Fe is observed. Because of the relevant environmental importance of the Fe particles, mainly due to their reactivity (chemical composition and high surface area) and size (mobility), more investigations are needed to better explore the relationships between Fe particles and tufa precipitation and dissolution. In the solid layer formation, are the nanoparticles incorporated into the bulk of the precipitate? Or does the precipitate grow keeping them

on the surface? This could imply that the concentration of Fe can be limited to the surface of the precipitates and not to its mass.

5.3 Dynamics of tufa precipitation in the Estero Morales

Observation of photos collected over an entire winter season in the Estero Morales reveals that tufa begins to grow on the channel bed as soon as the discharge is reduced to below the threshold values, and conductivity increases due to the vanished glacial melt contribution to discharge. The tufa disappears as soon as the snow starts to melt at the beginning of spring and the increased flow has lower conductivity. The visual evidence of the relationship between water conductivity and tufa precipitation has also been reported by Domínguez-Villar et al. (2017) in the Trabaque River in Spain. However, higher electrical conductivity is not a primary and sufficient reason for calcite precipitation. In this case, higher conductivity is a consequence of higher dissolved calcium concentration, which along with temperature, alkalinity, and pH determine the conditions for calcite supersaturation. The thermodynamic feasibility of calcite precipitation or dissolution, assessed by the calcite saturation index, was found to shift between supersaturation and subsaturation conditions for the Estero Morales. For these reasons, we hypothesize that a combination of high shear stress due to higher flows (i.e., abrasion) and changes in water chemistry (i.e., temperature, pH, alkalinity and calcium) trigger the disappearance of

tufa from the Estero Morales. However, the continuous monitoring of a wider range of physicochemical and biological parameters would allow one to gain further (bio)geochemical insight into tufa formation and disappearance, which at the moment is only partially understood.

5.4 Relevance and implications

The field investigation on the Estero Morales revealed that tufa precipitation undergoes complex dynamics of formation and vanishing, most likely related to changes of discharge, water temperature and conductivity. In glacial environments such as the Estero Morales, under climatic threat because of the progressive reduction in the glacier surface (Milner et al., 2017), and the projected temperature increase (Huss et al., 2017), the dynamics of tufa are likely to be affected. This would probably result in a longer period of tufa precipitation in the channel bed, with geomorphological implications in terms of sediment transport, long-term channel evolution, hyporheic flows, and changes in the downstream rivers. Moreover, increases in temperature could facilitate the growth of algae and cyanobacteria, creating thicker biofilm layers over the sediments (Díaz Villanueva et al., 2010). As demonstrated by Pedley and Rogerson (2010), temperature strongly influences the composition of the biofilm community. Biofilms in aquatic environments can resist high flow (Vignaga et al., 2012) and their colonization may enhance sediment stabilization (Fang et al.,

2014). The effectiveness of extracted extracellular polymeric substances (EPSs) on sediment stability was also demonstrated to be sensitive to environmental conditions such as salinity, pH and temperature (Van de Lageweg et al., 2018). Thus, one could expect that the combined effect of tufa precipitation and biofilms may lead to greater geomorphological stability (Batalla and Vericat, 2009). In excess, it can result in negative ecological effects, covering the whole riverbed and reducing the permeability of the sediment layer (Battin and Sengschmitt, 1999), resulting also in local changes of roughness (Piqué et al., 2016). Although the precipitate was not enriched in toxic metals or metalloids in this case, Fe oxyhydroxides are known by their affinity to As, Pb, Cu, Cd, etc. Thus, the presence or absence of the tufa layer may have implications for the fate of toxic species in mountain environments. However, a multidisciplinary physicochemical and biogeomorphological approach may be necessary to better understand the short- and long-term role that tufa and other contaminants have on sediment dynamics as well as the possible implications associated with natural processes (e.g., global climate change, biotic transformation, groundwater modifications).

6. Conclusions

In this study, we present the results of a series of field surveys and physical experiments conducted to analyze the implications of tufa precipitation on

sediment transport. The study was conducted in an Andean stream (Estero Morales) in which tufa precipitation creates a thin solid layer that covers the sediments along the wet channels of the river in winter.

It has been shown that tufa precipitation can influence the dynamics and mechanisms of sediment transport. Although more sediment flux is observed for finer sediments, when tufa precipitation is present in a heterogeneous mixture, it seems to enhance sediment stabilization. Moreover, we demonstrated that the influence of tufa precipitation on sediment entrainment is approximately three times larger, than that of biota and biofilms. To date, very little evidence has shown the impact of contaminants on river dynamics. However, more studies are needed for a complete analysis of the impact of contaminants on sediment entrainment and transport. A more detailed analysis of the large–scale implications of local effects as well as the feedback of different contaminants should be taken into consideration. An effective and useful tool could be to combine field and physical evidence in order to develop numerical models that can simulate the role of contaminants on sediment entrainment and transport, thereby analyzing the temporal scale of the phenomenon and what kind of factors provide the dissolution of the solid layer. New techniques are most likely needed with prevailing in situ surveys in order to maintain the natural characteristics of the analyzed contaminants.

7. Acknowledgments

This work was supported by the projects Fondecyt Regular 1170657, 1161337, Fondecyt Postdoctorado 3170011, and Conicyt FONDAP Grants 15110017 and 15110020. We acknowledge Fernanda Carrasco for help with physicochemical measurements and Fondequip EQM150101 for use of the electron microscope at CIEN-UC. Enzo Montenegro and Alessandra Manca are also thanked for their help in the field and flume experiments.

References

Arce, G., Montecinos, M., Guerra, P., Escauriaza, C., Coquery, M., Pastén, P., 2017. Enhancement of particle aggregation in the presence of organic matter during neutralization of acid drainage in a stream confluence and its effect on arsenic immobilization. Chemosphere 180, 574–583. doi:10.1016/j.chemosphere.2017.03.107.

Arenas, C., Gutiérrez, F., Osácar, C., Sancho, C., 2000. Sedimentology and geochemistry of fluvio-lacustrine tufa deposits controlled by evaporite solution subsidence in the central Ebro Depression, NE Spain. Sedimentology 47, 883–909.

Arenas, C., Vázquez-Urbez, M., Auqué, L., Sancho, C., Osácar, C., Pardo, G., 2014. Intrinsic and extrinsic controls of spatial and temporal variations in modern fluvial tufa sedimentation: A thirteen-year record from a semi-arid environment. Sedimentology 61, 90–132.

Arenas, C., Vázquez-Urbez, C., Pardo-Tirapu, G., Sancho-Marcén, C., 2010. Fluvial and associated carbonate deposits. In Carbonates in continental settings: Facies, Environments and Processes. Alonso-Zarza A.M., Tanner L.H. (eds), Developments in Sedimentology 61, 133–175.

Batalla, R.J., Vericat, D., 2009. Hydrological and sediment transport dynamics of flushing flows: implications for management in large Mediterranean rivers. River Research and Applications 25 (3), 297–314. doi:10.1002/rra.1160.

Bathurst, J.C., Graf, W.H., Cao, H.H., 1987. Bed load discharge equations for steep mountain rivers, in Sediment Transport in Gravel-Bed Rivers, edited by C. R. Thorne, J. C. Bathurst, and R. D. Hey, 453–477, John Wiley, New York.

Battin, T.J., Sengschmitt, D., 1999. Linking sediment biofilms, hydrodynamics, and river bed clogging: evidence from a large river. Microbial Ecology 37, 185–196. doi:10.1007/s002489900142.

Bauer, M., Blodau, C., 2009. Arsenic distribution in the dissolved, colloidal and particulate size fraction of experimental solutions rich in dissolved organic matter and ferric iron. Geochimica et Cosmochimica Acta 73, 529–542. doi:10.1016/j.gca.2008.10.030.

Bolhassani, R., Afzalimehr, H., Subhasish, D., 2015. Effects of relative submergence and bed slope on sediment incipient motion under

decelerating flows. Journal of Hydrology and Hydromechanics 63 (4), 295–302. doi:10.1515/johh-2015-0039.

Buffington, J., Montgomery, D., 1997. A systematic analysis of eight decades of incipient motion studies, with special reference to gravel-bedded rivers. Water Resources Research 33, 1993–2029.

Bugueño, M., Acevedo, S., Bonilla, C., Pizarro, G., Pasten, P., 2014. Differential arsenic binding in the sediments of two sites in Chile's lower Loa River basin. Science of the Total Environment 466, 387–396. DOI: 10.1016/j.scitotenv.2013.06.114.

Bunte, K., Abt, S.R., Swingle, K.W., Cenderelli, D.A., Schneider, J.M., 2013. Critical Shields values in coarse-bedded steep streams, Water Resources Research. 49, 7427–7447. doi:10.1002/2012WR012672.

Buxton, T.H., Buffington, J.M., Yager, E.M., Hassan, M.A., Fremier, A.K., 2015. The relative stability of salmon redds and unspawned streambeds, Water Resources Research. 51, 6074–6092. doi:10.1002/2015WR016908.

Capezzuoli, E., Gandin, A., Pedley, M., 2014. Decoding tufa and travertine (fresh water carbonates) in the sedimentary record: the state of the art. Sedimentology 61, 1–21.

Carthew, K.D., Taylor, M.P., Drysdale, R.N., 2003. Are current models of tufa sedimentary environments applicable to tropical systems? A case study from the Gregory River. Sedimentary Geology 162, 199–218.

Cheng, W., Fang, H., Lai, H., Huang, L., Dey, S., 2017. Effects of biofilm on turbulence characteristics and the transport of fine sediment. Journal of Soils and Sediments. doi:10.1007/s11368-017-1859-1.

Cyr, H., Morton, K.E., 2006. Distribution of biofilm exopolymeric substances in littoral sediments of Canadian Shield lakes: the effects of light and substrate. Canadian Journal of Fisheries and Aquatic Sciences 63, 1763–1776. doi:10.1139/F06-079.

Díaz Villanueva, V., Font, J., Schwartz, T., Romaní, A.M., 2010. Biofilm formation at warming temperature: acceleration of microbial colonization and microbial interactive effects. Biofouling 27(1), 59–71. doi:10.1080/08927014.2010.538841.

Domínguez-Villar, D., Vázquez-Navarro, J.A., Krklec, K., 2017. The role of gypsum and/or dolomite dissolution in tufa precipitation: Lessons from the hydrochemistry of a carbonate–sulphate karst system. Earth Surface Processes and Landforms 42 (2), 245–258.

Drysdale, R.N., Taylor, M.P., Ihlenfeld, C., 2002. Factors controlling the chemical evolution of travertine-depositing rivers of the Barkly karst, northern Australia. Hydrological Processes 16, 2941–2962.

EPA, U. S., 2007a. Method 3051A. Microwave-assisted acid digestion of sediments, sludges, soils and oils (pp 1–14). Technical Report, Washington, District of Columbia.

EPA, U. S., 2007b. Method 3015A (SW-846): Microwave Assisted Acid Digestion of Aqueous Samples and Extracts: EPA Washington DC.

Fang, H.W., Lai, H.J., Cheng, W., Huang, L., He, G.J., 2017. Modeling sediment transport with an integrated view of the biofilm effects, Water Resources Research 53, 7536–7557. doi:10.1002/2017WR020628.

Fang, H.W., Shang, Q.Q., Chen, M.H., He, G.J., 2014. Changes in the critical erosion velocity for sediment colonized by biofilm. Sedimentology 61 (3), 648–659.

Ford, T.D., Pedley, H.M., 1996. A review of tufa and travertine deposits of the world. Earth-Science Reviews 41, 117–175.

Gerbersdorf, S.U., Jancke, T., Westrich, B., Paterson, D.M., 2008. Microbial stabilization of riverine sediments by extracellular poly- meric substances. Geobiology 6 (1), 57–69.

Gerbersdorf, S.U., Wieprecht, S., 2015. Biostabilization of cohesive sediments: revisiting the role of abiotic conditions, physiology and diversity of microbes, polymeric secretion, and biofilm architecture. Geobiology 13, 68–97.

Gottesfeld, A.S., Hassan, M.A., Tunnicliffe, J.F., Poirer, R.W., 2004. Sediment dispersion in salmon spawning streams: The influence of floods and salmon redd construction. Journal of the American Water Resources Association 40, 1071–1086.

Graba, M., Moulin, F.Y., Boulêtreau, S., Garabétian, F., Kettab, A., Eiff, O., Sánchez Pérez, J.M., Sauvage, S., 2010. Effect of near-bed turbulence on chronic detachment of epilithic biofilm: experimental and modelling approaches. Water Resources Research 46, 1–15.

Gradziński, M., 2010. Factors controlling growth of modern tufa: results of a field experiment. Geological Society Special Publication 336, 143–191.

Grant, J., Gust, G., 1987. Prediction of coastal sediment stability from photopigment content of mats of purple sulfur bacteria. Nature 330, 244–246.

Hamdouni, A., Montes-Hernandez, G., Tlili, M., Findling, F., Renard, C., Putnis C., 2016. Removal of Fe(II) from groundwater via aqueous portlandite carbonation and calcite-solution interactions. Chemical Engineering Journal 283, 401–411.

Huss, M., Bookhagen, B., Huggel, C., Jacobsen, D., Bradely, R.S., Clague, J.J., Vuille, M., Buytaert, W., Cayan, D.R., Greenwood, G., Mark, B.G., Milner, A.M., Weingartner, R., Winder, W., 2017. Toward mountains without permanent snow and ice. Earth's Future 5, 418–435. doi:10.1002/2016EF000514.

Johnson, M.F., Reid, I., Rice, S.P., Wood, P.J., 2009. Stabilization of fine gravels by net-spinning caddisfly larvae. Earth Surface Processes and Landforms 34, 413–423.

Kempe, S., Emeis, K., 1985. Carbonate chemistry and the formation of Plitvice Lakes. In Transport of Carbon and Minerals in Major World Rivers, Degens ET (ed.). University of Hamburg Sonderband No. 58. Geological–Palaeontological Institute, 351–383.

Kuhnle, R.A., 1993. Incipient motion of sand-gravel sediment mixtures. Journal of Hydraulic Engineering 119, 1400–1415. doi:10.1061/(ASCE)0733-9429(1993)119: 12(1400).

Lamb, M., Dietrich, W., Venditti, J., 2008. Is the critical shields stress for incipient sedimentmotion dependent on channel- bed slope?. Journal of Geophysical Research 113, F02008. doi:10.1029/2007JF000831.

Lee, H., Balachandar, S., 2012. Critical shear stress for incipient motion of a particle on a rough bed. Journal of Geophysical Research 117, F01026. doi:10.1029/2011JF002208.

Lu, G., Zheng, C., Donahoe, R.J., Berry, L.W., 2000. Controlling processes in a CaCO3 precipitating stream in Huanglong Natural Scenic District, Sichuan, China. Journal of Hydrology 230, 34–54.

Lundkvist, M., Grui, M., Friend, P.L., Flindt, M.R., 2007. The relative contributions of physical and microbiological factors to cohesive sediment stability. Continental Shelf Research 27, 1143–1152. doi:10.1016/J.CSR.2006.01.021.

Mao, L., Carrillo, R., 2017. Temporal dynamics of suspended sediment transport in a glacierized Andean basin. Geomorphology 287, 116-125.

Mao, L., Carrillo, R., Escauriaza, C., Iroume, A., 2016. Flume and field-based calibration of surrogate sensors for monitoring bedload transport. Geomorphology 253, 10–21.

Martini, I., Capezzuoli, E., 2014. Interdigitated fluvial clastic deposits and calcareous tufa testifying an uplift of the catchment area: An example from the Pianizzoli. Sedimentary Geololy 299, 60–73. doi: 10.1016/j.sedgeo.2013.11.001.

Milner, A.M, Khamis, K., Battin, T.J., Brittain, J.E., Barrand, N.E., Füreder, L., Cauvy-Fraunié, S., Gíslason, G.M., Jacobsen, D., Hannah, D.M., Hodson, A.J., Hoodk, E., Lencioni, V., Ólafsson, J.S., Robinson, C.T., Tranter, M., Brown, L.E., 2017. Glacier shrinkage driving global changes in downstream systems. Proceedings of the National Academy of Sciences of the United States of America 114 (37), 9770–9778. doi:10.1073/pnas.1619807114.

Naiman, R.J., Elliott, S.R., Hellfield, J.M., O'Keefe, T.C., 2000. Biophysical interactions and the structure and dynamics of riverine ecosystems: the importance of biotic feedbacks. Hydrobiologia 410, 79–86.

Ordóñez, S., Benavente, D., 2014. Revisión de los modelos hidrogeoquímicos de génesis de tobas calcáreas. Estudios Geológicos 70 (2), e013.

Parkhurst, D.L., Appelo, C.A.J. (2013). Description of input and examples for PHREEQC version 3. A computer program for speciation, batch reaction, one dimensional transport, and inverse geochemical calculations. In: U.S. Geological Survey (Ed.), Techniques and Methods. U.S. Geological Survey, Denver, Colorado (Book 6, Chap. A43).

Pedley, H.M., 1990. Classification and environmental models of cool freshwater tufas. Sedimentary Geology 68, 143–154.

Pedley H.M., 2009. Tufas and travertines of the Mediterranean region: a testing ground for freshwater carbonate concepts and developments. Sedimentology 56, 221–246.

Pedley, H.M., Rogerson, M., 2010. In vitro investigations of the impact of different temperature and flow velocity conditions on tufa microfabric. In: Speleothems and Tufas: Unravelling Physical and Biological controls, edited by: Pedley, H.M., Rogerson, M., Geological Society Special Publication, Geological Society of London, London, 193–210.

Pedley, H.M., 2014. The morphology and function of thrombolitic calcite precipitating biofilms: A universal model derived from freshwater mesocosm experiments. Sedimentology 61, 22–40.

Piqué, G., Vericat, D., Sabater, S., Batalla, R.J., 2016. Effects of biofilm on river-bed scour. Science of the Total Environment 572, 10–1046. doi:10.1016/j.scitotenv.2016.08.009.

Pledger, A.G., Rice, S.P., Millett, J., 2014. Reduced bed material stability and increased bedload transport caused by foraging fish: a flume study with juvenile Barbel (Barbus barbus). Earth Surface Processes and Landforms 39, 1500–1513.

Rice, S.P., Johnson, M.F., Reid, I., 2012. Animals and the geomorphology of gravel-bed rivers. In Gravel-bed Rivers: Processes, Tools, Environments, Church M, Biron P, Roy AG (eds). John Wiley & Sons: Chichester, 225–241.

Riding, R., 1979. Origin and diagenesis of lacustrine algal bioherms at the margin of the Ries crater, Upper Miocene, southern Germany. Sedimentology 26, 645–680.

Righetti, M., Lucarelli, C., 2007. May the Shields theory be extended to cohesive and adhesive benthic sediments? Journal of Geophysical Research: Oceans 112:C05039, 1–14. doi:10.1029/2006JC003669.

Rupp, G.L., Adams, V.D., 1981. Calcium Carbonate Precipitation as Influenced by Stream Primary Production. Reports. Paper 116.

Schmeeckle, M.W., Nelson J.M., 2003. Direct simulation of bedload transport using a local, dynamic boundary condition. Sedimentology 50 (2), 279–301. doi:10.1046/j.1365-3091.2003.00555.x.

Shields, A., 1936. Application of similarity principles and turbulence research to bed-load movement," in W.P. Ott and J.C. Uchelen

(Translators), Hydrodynamics Laboratory Publication, Report No. 167, California Institute of Technology, Pasadena, CA.

Shvidchenko, A.B., Pender, G., Hoey, T.B., 2001. Critical shear stress for incipient motion of sand/gravel streambeds. Water Resources Research 37 (8), 2273–2283. doi:10.1029/2000WR000036.

Stone, M., Emelko, M.B., Droppo, I.G., Silins, U., 2011. Biostabilization and erodibility of cohesive sediment deposits in wildfire-affected streams. Water Research 45(2), 521–534.

Thom, M., Schmidt, H., Gerbersdorf, S.U., Wieprecht, S., 2015. Seasonal biostabilization and erosion behavior of fluvial biofilms under different hydrodynamic and light conditions. International Journal of Sediment Research 30, 273–284.

Toker, E., 2017. Quaternary Fluvial Tufas from Sarikavak Area, Denizli, Southwestern Turkey: Palaeoenvironmental and Palaeoclimatic Implications. Quaternary International, Non-marine Carbonates, Special Issue 437 (PA) 51-70.

Turner, E.C., James, N.P., Narbonne, G.M., 2000. Taphonomic control on microstructure in Early Neoproterozoic reefal stromatolites and thrombolites. Palaios 15, 87–111.

Underwood, G.J.C., Peterson, D.M., 2003. The importance of extracellular carbohydrate production by marine epipelic diatoms. Advances in Botanical Research 40, 183–240.

Vacca, C., Mao, L., Dominici, R., Carrillo, R., 2016. Sensitivity analysis of the parameters of the Erosion Potential Method: the case of the Estero Morales, Chile. 88° Congresso della Societá Geologica Italiana. Naples, 7-9 September.

Van de Lageweg, W.I., McLelland, S.J., Parsons, D.R., 2018. Quantifying biostabilisation effects of biofilm-secreted and extracted extracellular polymeric substances (EPSs) on sandy substrate, Earth Surface Dynamics 6, 203–215. doi:10.5194/esurf-6-203-2018.

Vázquez-Urbez, M., Arenas, C., Sancho, C., Osácar, C., Auqué, L., Pardo, G., 2010. Factors controlling present –day tufa dynamics in the Monasterio de Piedra Natural Park (Iberian Range, Spain): depositional environmental settings, sedimentation rates and hydrochemistry. International Journal of Earth Sciences (Geol. Rundsch) 99, 1027–1049.

Vignaga, E., 2012. The Effect of Biofilm Colonization on the Stability of Non-Cohesive Sediments Unpublished PhD Thesis University of Glasgow, 263p.

Vignaga, E., Haynes, H., Sloan, W.T., 2012. Quantifying the tensile strength of microbial mats grown over noncohesive sediments. Biotechnology and Bioengineering 109, 1155–1164. doi :10.1002/bit.24401.

Vignaga, E., Sloan, D.M., Luo, X., Haynes, H., Phoenix, V.R., Sloan, W.T., 2013. Erosion of biofilm-bound fluvial sediments. Nature Geoscience 6, 770–774. doi:10.1038/ngeo1891.

White, W.B., 2010. Springwater geochemistry. In Groundwater Hydrology of Springs. Engineering, Theory, Management, and Sustainability, Kresic N, Stevanovic Z (eds). Butterworth-Heinemann/Elsevier: Burlington, 231–268.

Tables caption

Tab. 1. Main characteristics of the boxes and parameters of the flume experiments.

Figure caption

Fig. 1. Map of the Estero Morales basin with locations of the San Francisco glacier, the "Aguas Panimávida" spring and the study site (on the left) and the generalized geological map of the basin (on the right).

Fig. 2. Views of the Estero Morales during the winter season, showing the golden aspect of the surface sediments in the wetted channel (a). Example of sediment covered by a thick (1-2 mm) layer of calcium carbonate precipitation (b), either boulders (c) and very fine sediments in the little bars (d). "Aguas Panimávida" spring present in Estero Morales during the entire year (e), river bank with tufa precipitation (f).

Fig. 3. Boxes with sediment without tufa precipitate placed along the main channel (a); Flume experiment 10-b using sediments without tufa precipitate (b).

Fig. 4. Analyses of three precipitate samples collected along the Estero Morales. (a) XRD patterns of the samples compared with the characteristic

angles and intensities of calcite (peaks labeled with C) and quartz (peaks labeled with Q), and (b) FTIR spectra of the samples compared with a calcite standard.

Fig. 5. View looking vertically down onto the base of tufa precipitate. Photomicrographs collected during the SEM analysis: porous rough surface of the precipitate (a); example of diatoms and bacteria on the precipitate surface (b and c, respectively); clusters of globular nanoparticles (d); characteristic EDS of the precipitate (e).

Fig. 6. Photomicrograph of tufa precipitate collected with FE SEM-EDS. Clusters of globular nanoparticles are the highlights in A, B, C and D. No evidence of Fe in areas without nanoparticles is reported in A and B. Associations of Fe with nanoparticles are visible in C and D.

Fig. 7. Peak push forces needed to entrain sediments with and without a tufa precipitation layer. The solid line indicates the range between the 25^{th} and 75^{th} percentiles, the square icon indicates the median, the whiskers indicate the maximum and minimum nonoutlier values, and the solid circles indicate outliers.

Fig. 8. Difference in peak push forces needed to entrain sediments with tufa precipitation layer cover distributed on diametric classes. The solid line indicates the range between the 25^{th} and 75^{th} percentiles, the square icon indicates the median, the whiskers indicate the maximum and minimum nonoutlier values, and the solid circles indicate outliers.

Fig. 9. Dimensional transport rate per unit width (q^*) against the dimensionless shear stress (τ^*) for the experiment with and without a tufa precipitation layer.

Fig. 10. Difference in sediment transport rate for unit width with and without a tufa precipitation layer for each sediment diameter.

Fig. 11. Cumulated number of sediments moved with and without a tufa precipitation layer for experiment 16-b.

Fig. 12. Period when tufa precipitation is present along the main channel of the Estero Morales River during 2015 in relation to conductivity and water discharge data: main channel without tufa precipitation (a), tufa precipitation begins to appear (b), tufa precipitation is developing (c), reaches its peak quantity (d), then it begins to disappear (e), leaving the main channel again (f).

Tab. 1. Main characteristics of the boxes and parameters of the flume experiments.

Code	Diameter (mm)	Data installation	N. of days installed	Slope (m/m)	N. runs	Time of exp. (sec)	τ (min-max)
4-a	4	16-08-2017	37	0.005	9	41	0.003-0.031
4-b	4	16-08-2017	43	0.005	9	40	0.003-0.034
8-a	8	05-07-2017	65	0.010	13	260	0.003-0.047
8-b	8	16-08-2017	37	0.010	16	88	0.002-0.047
8-c	8	16-08-2017	12	0.010	16	87	0.003-0.048
16-a	16	16-08-2017	41	0.015	14	92	0.003-0.049
16-b	16	05-07-2017	65	0.015	21	325	0.003-0.053
10-a	10	08-08-2017	31	0.015	12	173	0.002-0.036
10-b	10	16-08-2017	37	0.015	9	83	0.003-0.037

Highlights

1. Tufa precipitation increases the critical shear stress for sediment entrainment

2. Greater force is needed to move sediment particles affected by tufa precipitation

3. Complex dynamics of formation and vanishing of tufa precipitation

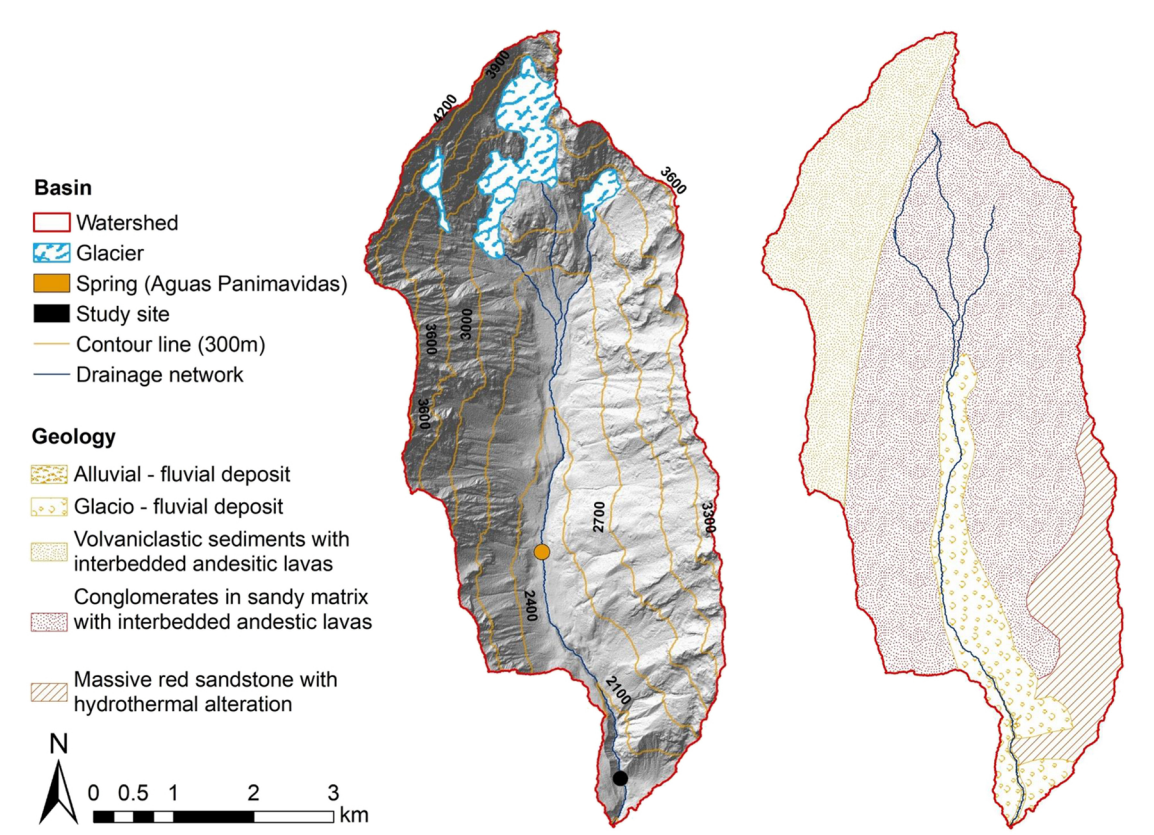
Basin
Watershed
Glacier
Spring (Aguas Panimavidas)
Study site
Contour line (300m)
Drainage network
Geology
Alluvial - fluvial deposit
Glacio - fluvial deposit
Volvaniclastic sediments with interbedded andesitic lavas
Conglomerates in sandy matrix with interbedded andestic lavas
Massive red sandstone with hydrothermal alteration
N
0 0.5 1 2 3
km
4200
3900
3600
3000
3600
3600
2700
3300
2400
2100

Figure 1

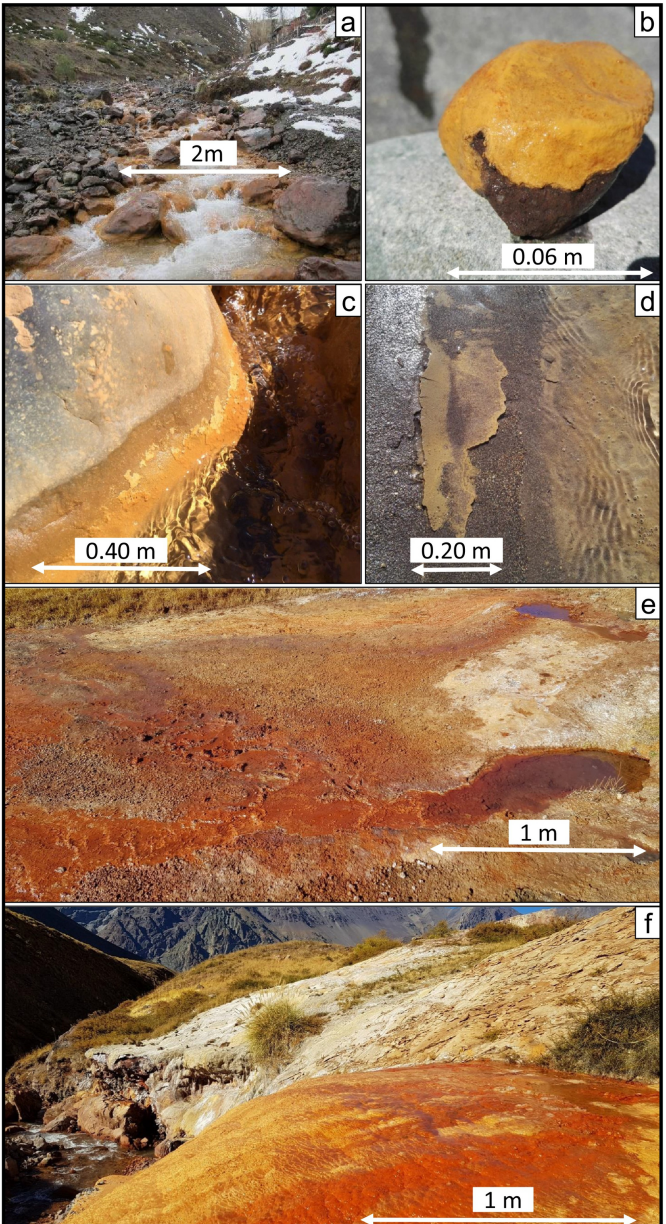

Figure 2

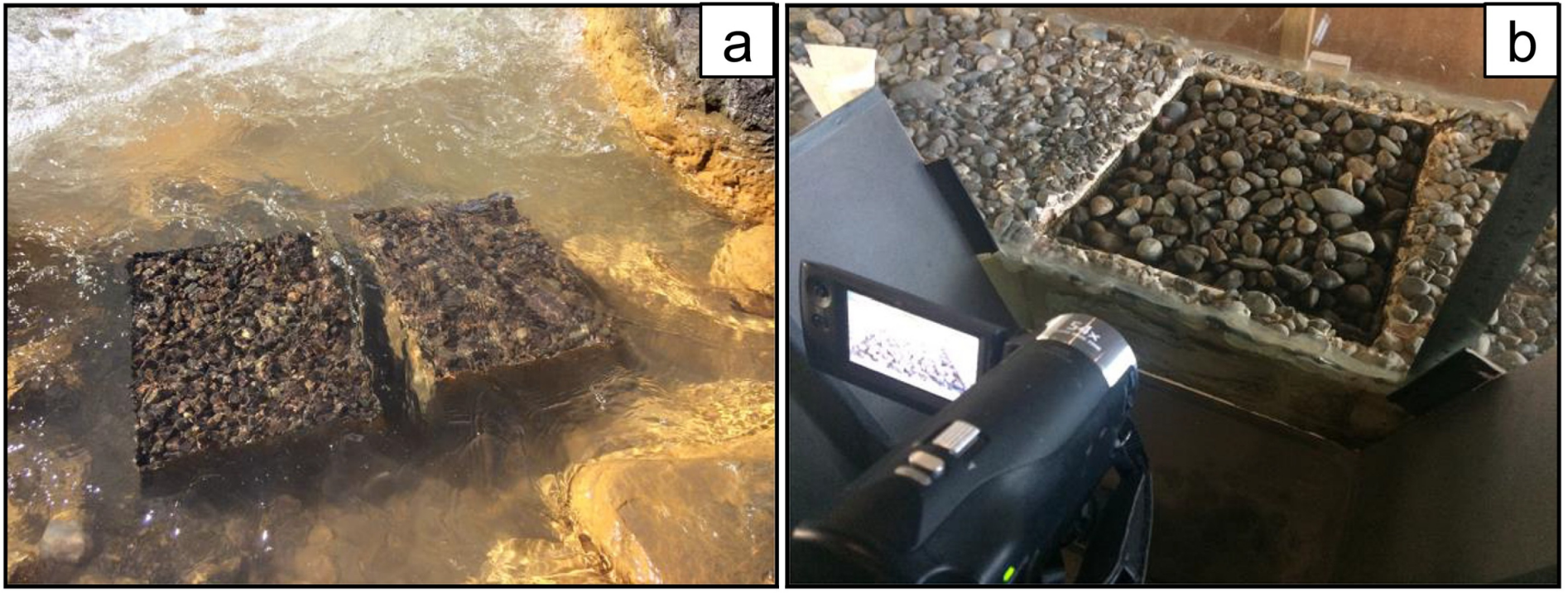

Figure 3

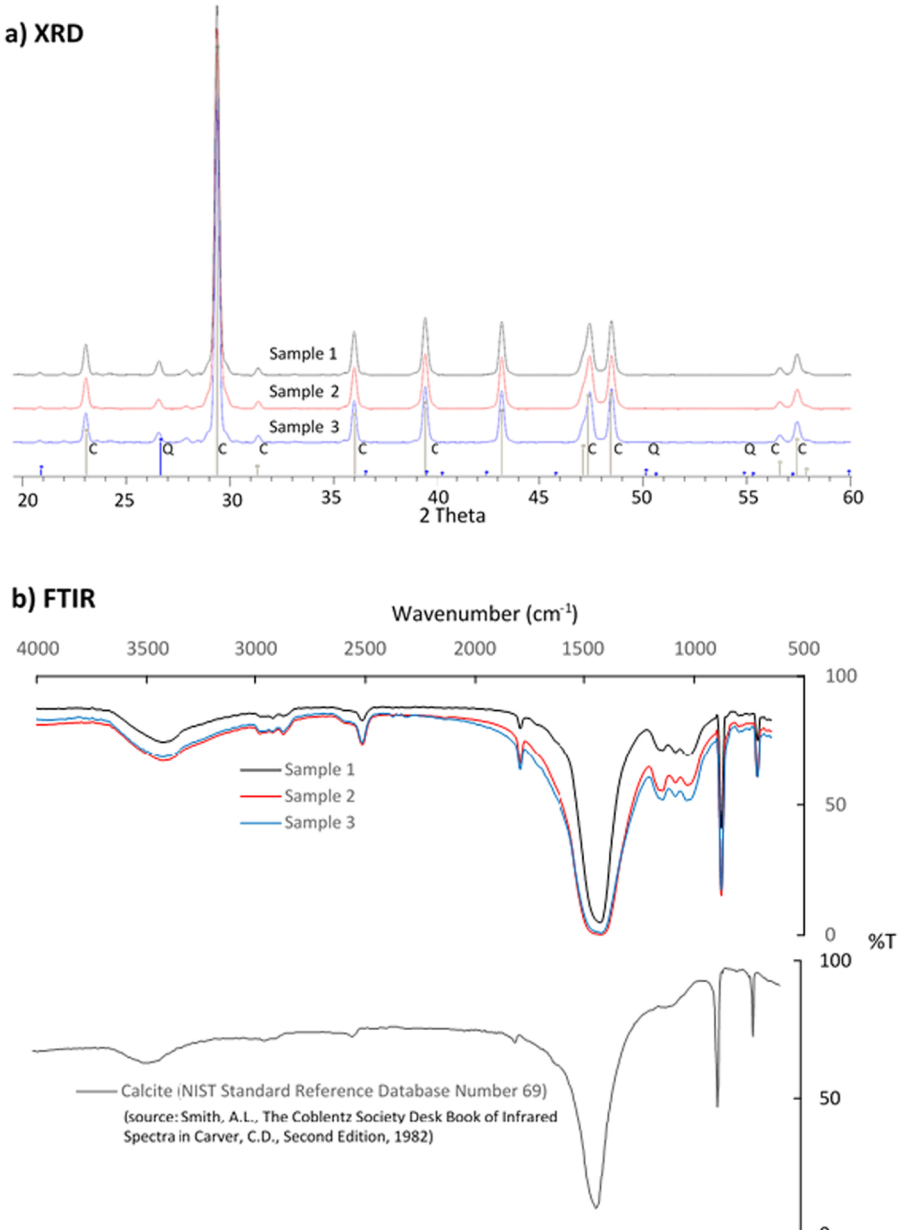
a) XRD
Sample 1
Sample 2
Sample 3
C
Q
C
C
C
C
C
C
Q
Q
C
C
20
25
30
35
40
45
50
55
60
2 Theta
b) FTIR
Wavenumber (cm-1)
4000
3500
3000
2500
2000
1500
1000
500
Sample 1
Sample 2
Sample 3
100
50
0
%T
Calcite (NIST Standard Reference Database Number 69)
(source: Smith, A.L., The Coblentz Society Desk Book of Infrared Spectra in Carver, C.D., Second Edition, 1982)
100
50
0

Figure 4

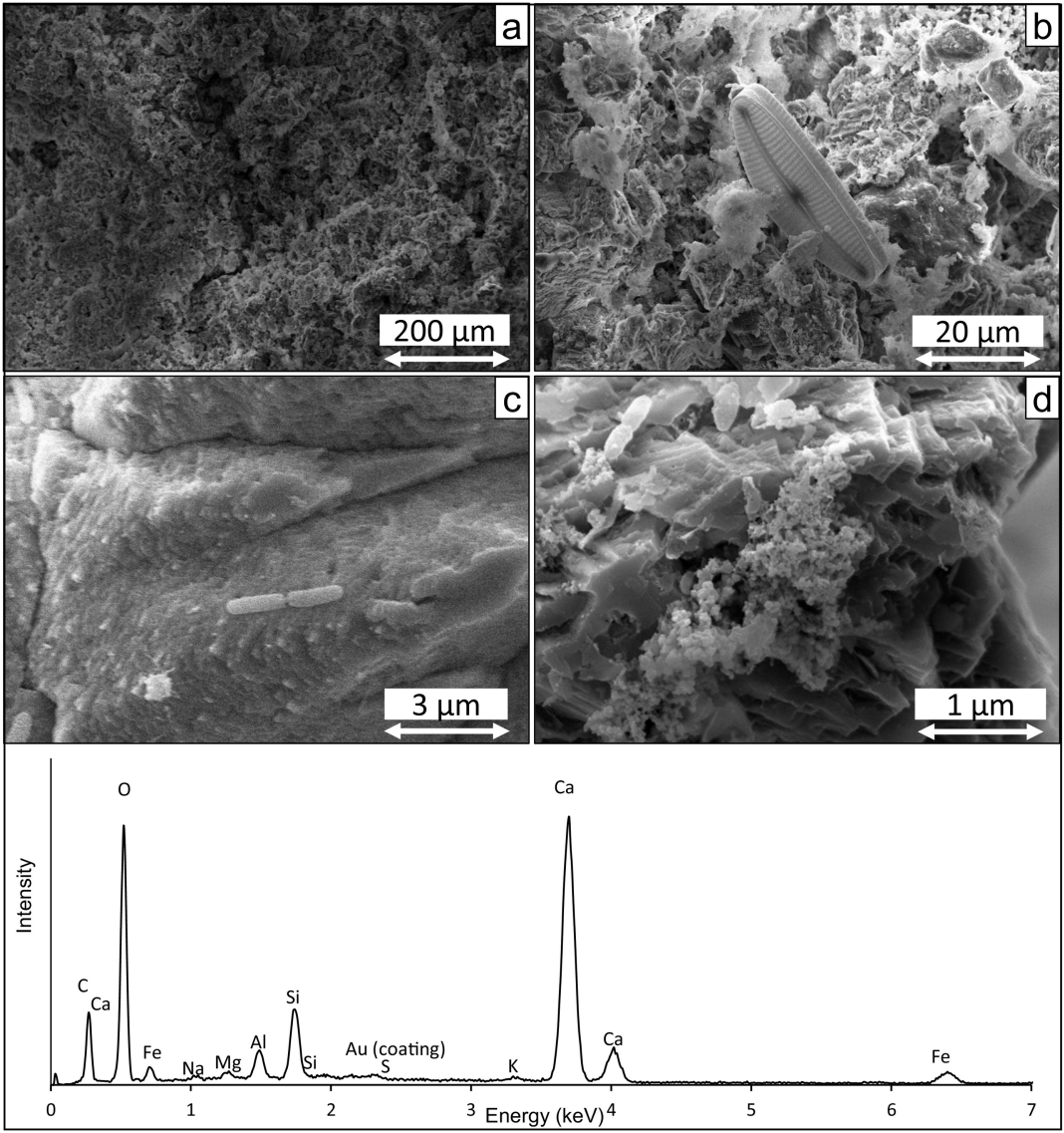
a
200 µm
b
20 µm
c
3 µm
d
1 µm
Intensity
O
Ca
C
Ca
Fe
Na
Mg
Al
Si
Si
Au (coating)
S
K
Ca
Fe
0
1
2
3
4
5
6
7
Energy (keV)

Figure 5

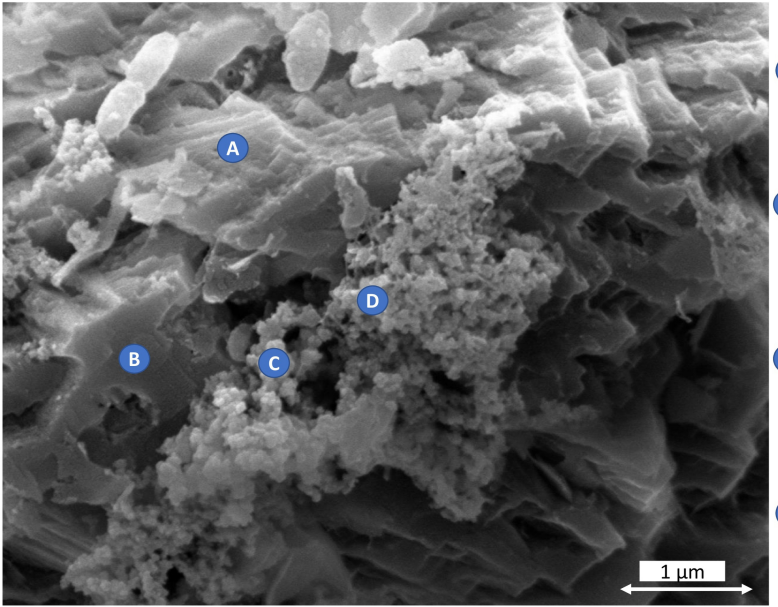

A

Element	Weight %	Atomic %
C	8.26	14.75
O	47.12	63.17
Si	1.08	0.82
Au	4.8	0.52
Ca	38.75	20.74

B

Element	Weight %	Atomic %
C	6.71	12.77
O	41.62	59.51
Al	0.78	0.66
Si	1.56	1.27
Au	5.2	0.6
Ca	44.14	25.19

C

Element	Weight %	Atomic %
C	7.11	14.09
O	38.62	57.52
Al	0.78	0.69
Si	1.81	1.54
Au	7.63	0.92
Ca	38.42	22.84
Fe	5.64	2.4

D

Element	Weight %	Atomic %
C	8.16	15.19
O	43.09	60.19
Al	0.72	0.6
Si	1.49	1.19
Au	5.06	0.57
Ca	36.01	20.08
Fe	5.46	2.18

Figure 6

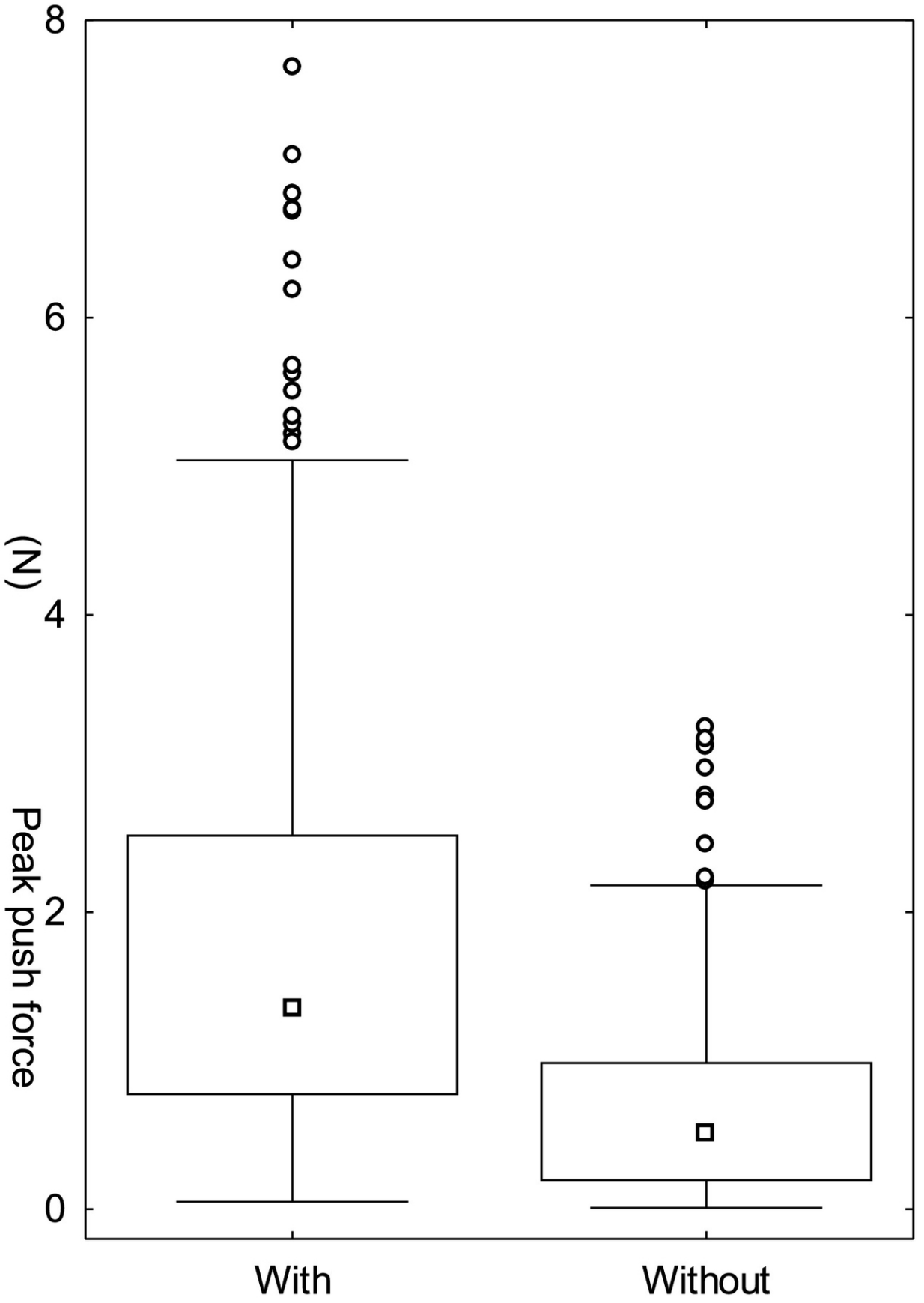

Figure 7

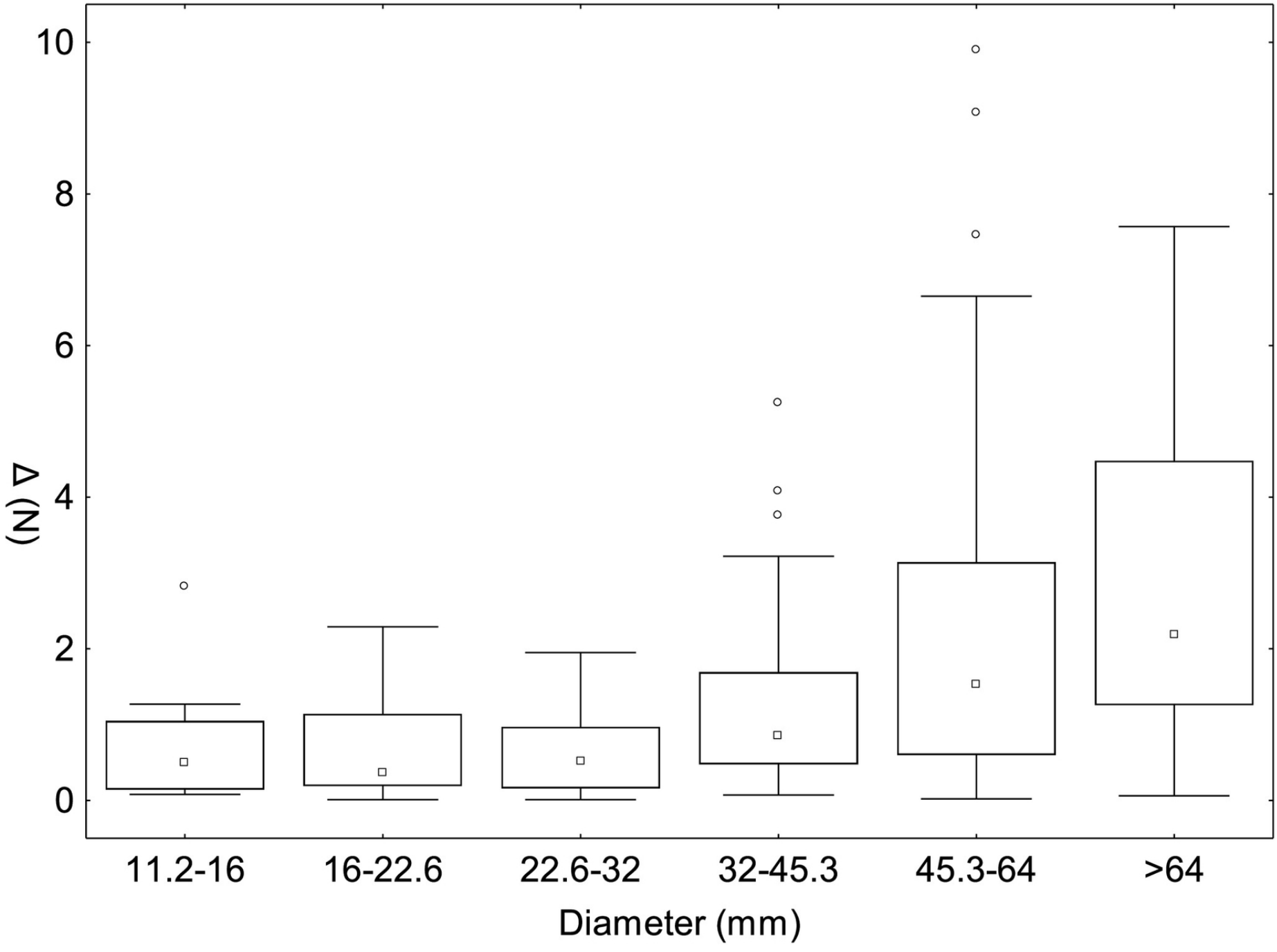

Figure 8

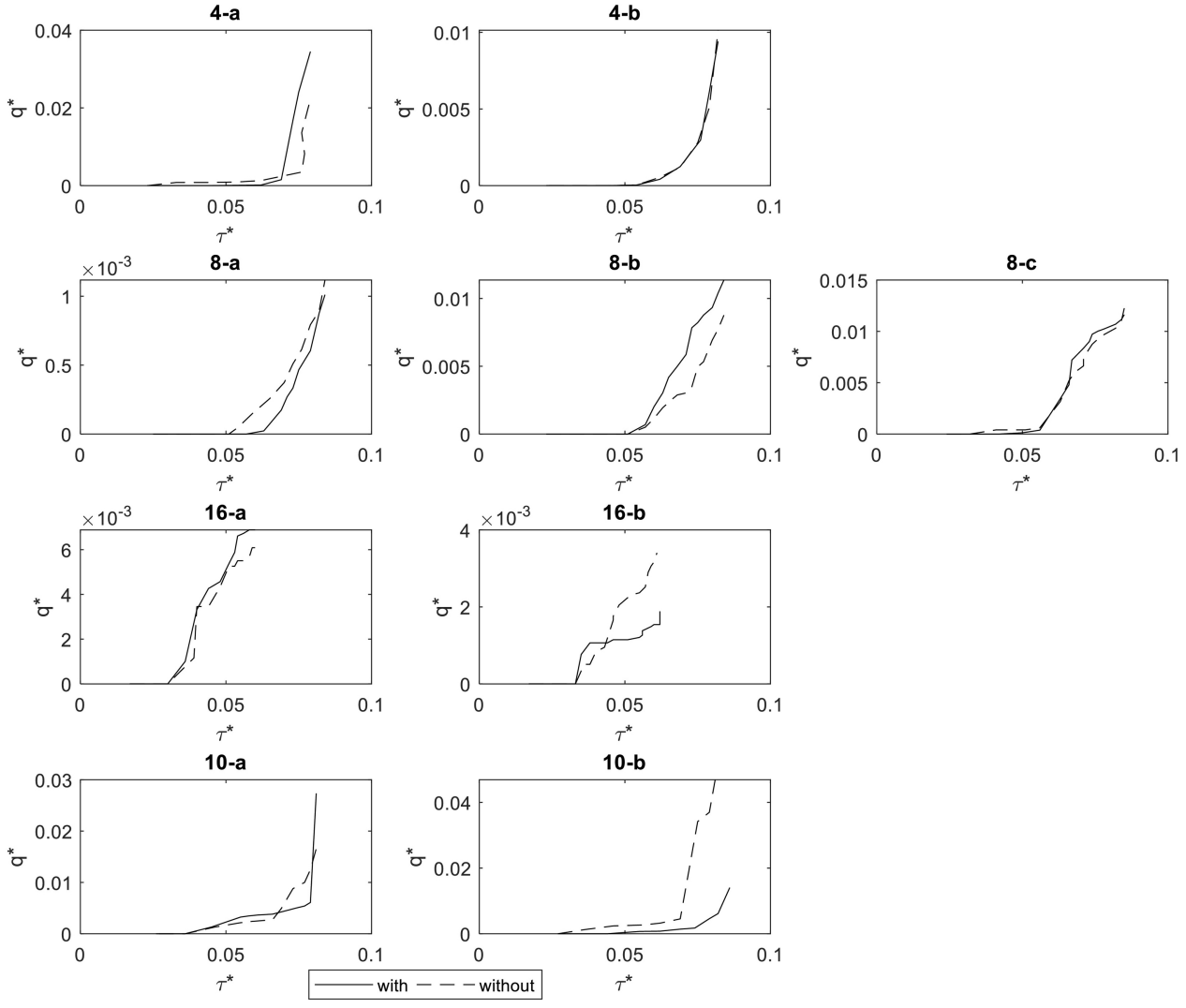

Figure 9

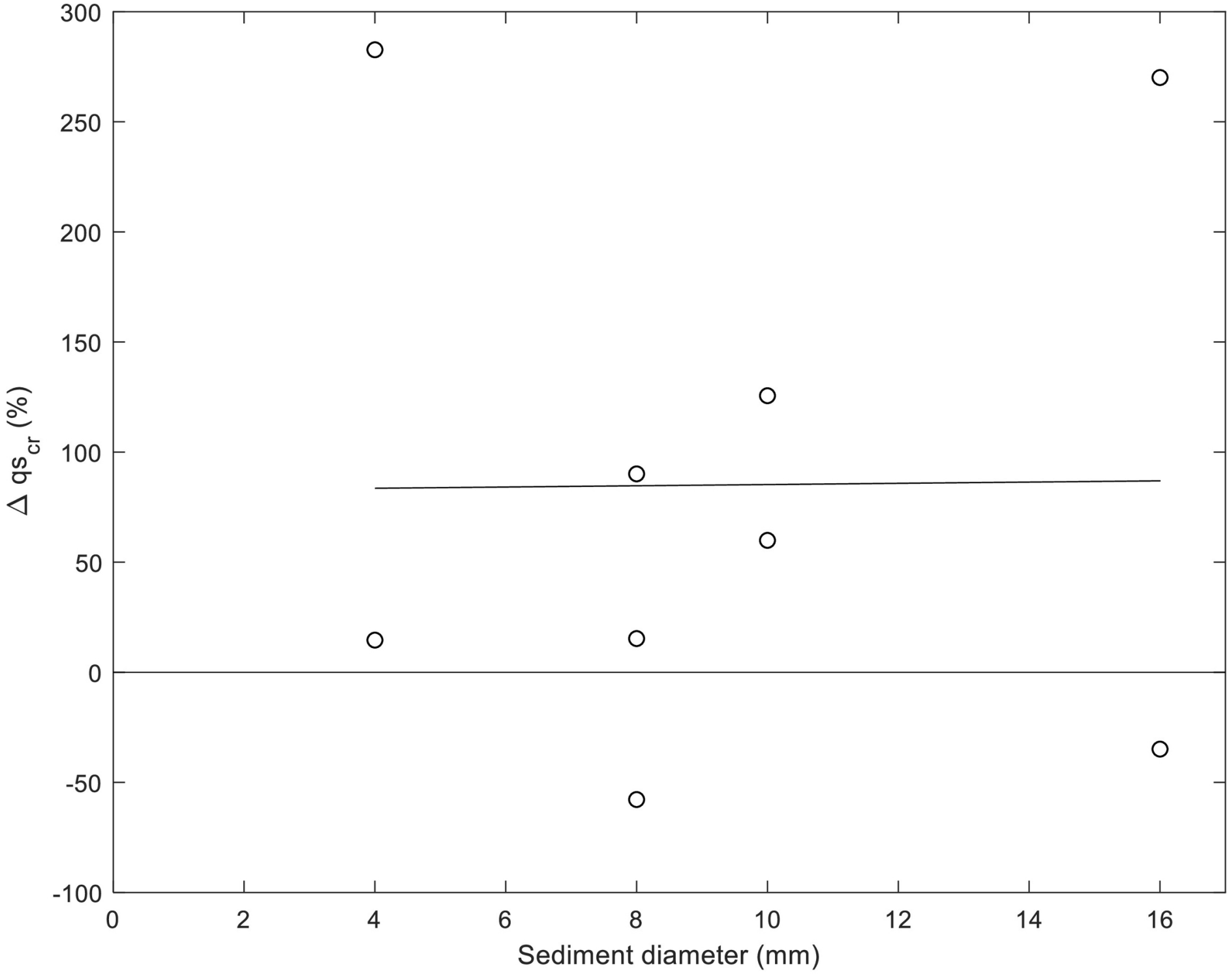
300
250
200
150
100
50
0
-50
-100
0
2
4
6
8
10
12
14
16
Δ qs$_{cr}$ (%)
Sediment diameter (mm)

Figure 10

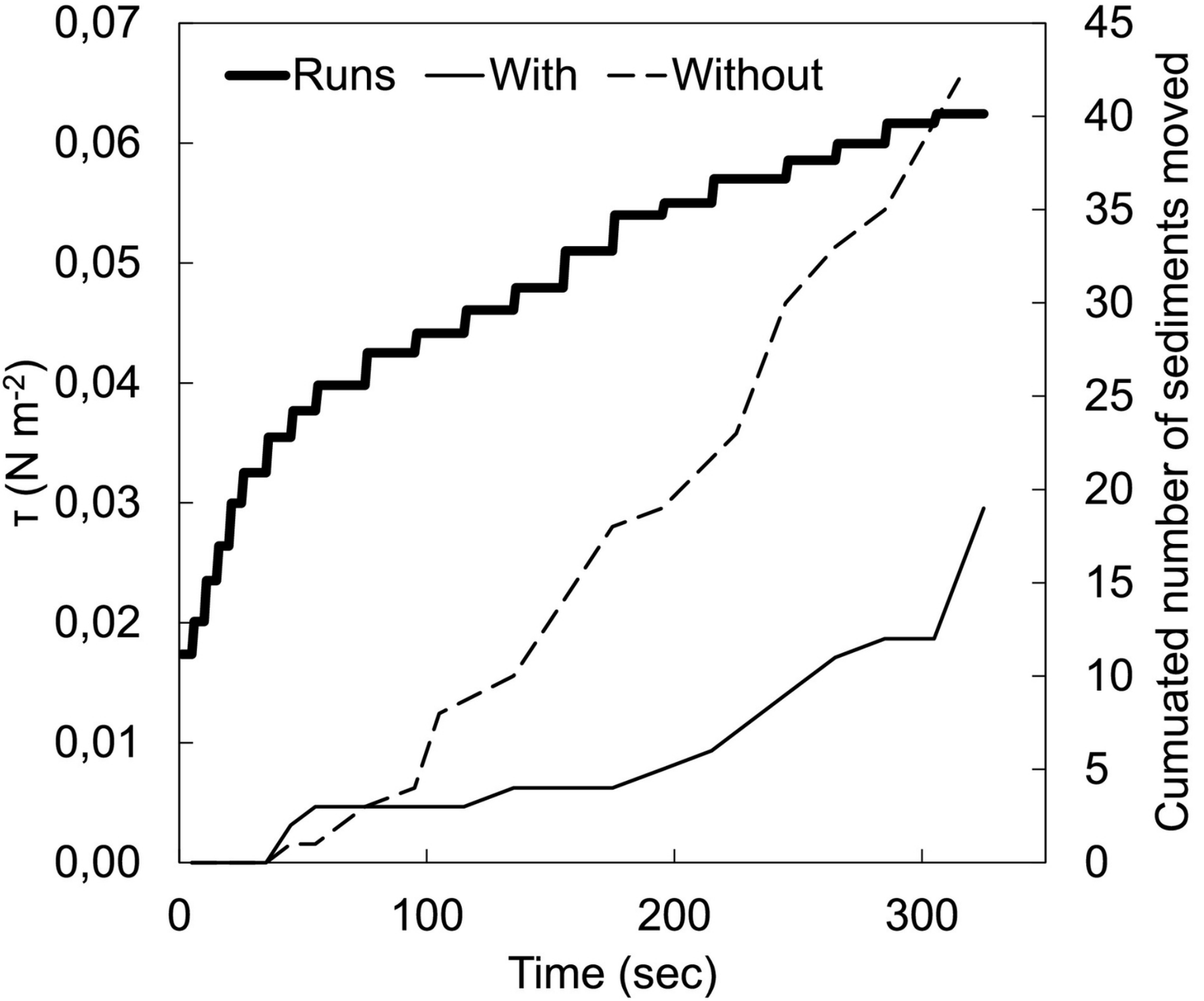
Runs
With
Without
0,07
0,06
0,05
0,04
0,03
0,02
0,01
0,00
τ (N m-2)
45
40
35
30
25
20
15
10
5
0
Cumuated number of sediments moved
0
100
200
300
Time (sec)

Figure 11

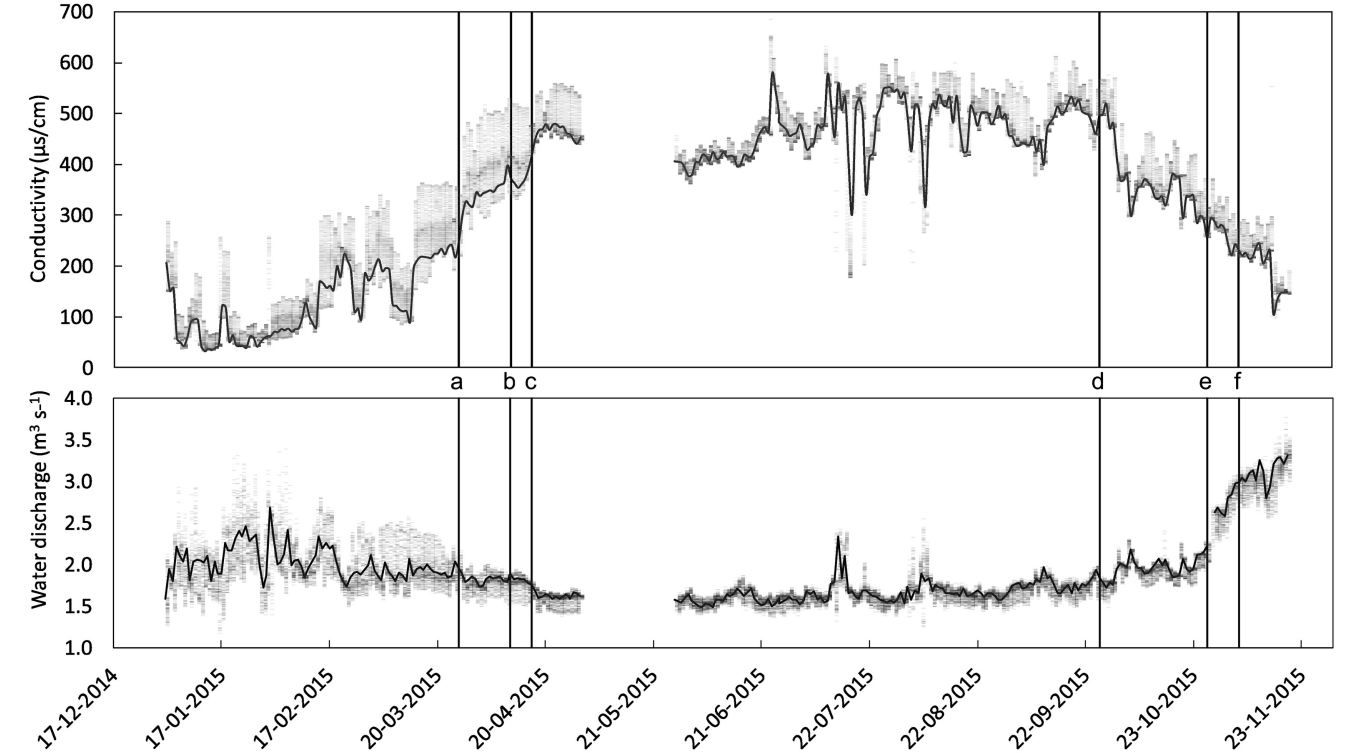
Conductivity (µs/cm)
700
600
500
400
300
200
100
0
a
b
c
d
e
f
Water discharge (m³ s⁻¹)
4.0
3.5
3.0
2.5
2.0
1.5
1.0
17-12-2014
17-01-2015
17-02-2015
20-03-2015
20-04-2015
21-05-2015
21-06-2015
22-07-2015
22-08-2015
22-09-2015
23-10-2015
23-11-2015

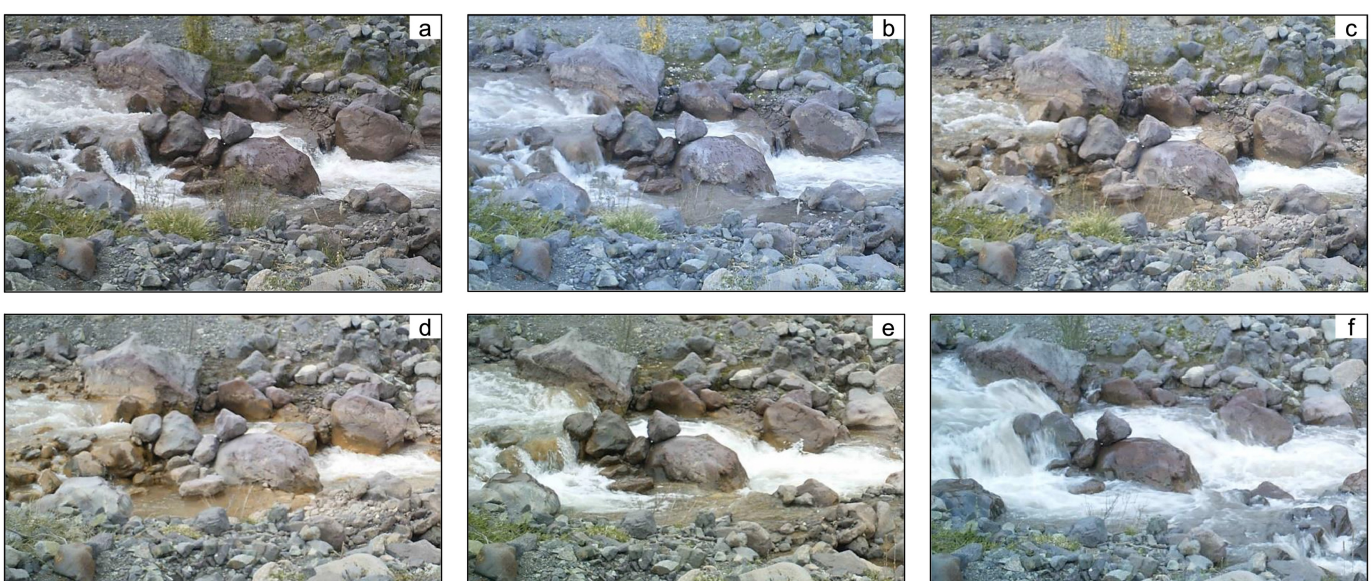
a
b
c
d
e
f

Figure 12